INTEGRAL MODEL WITH MACHINE LEARNING FOR BALANCING HEAT TRANSFER AND ENERGY GENERATION IN ALGAL BIO-REACTIVE FAÇADES

Adham M. Elmalky[1], and Mohamad T. Araji[2]
[1]Mechanical and Mechatronics Engineering, University of Waterloo, Waterloo, Canada
[2]School of Architecture, University of Waterloo, Cambridge, Canada

ABSTRACT

Microalgae bioreactors represent one renewable energy source that has heat generation capacity in addition to dynamic conversion of light to biomass all year round. If integrated into double-skin façades, the assembly can create building synergies by linking different systems for energy and heat distribution in cold climates. For this purpose, a new integral model was developed by coupling *MATLAB*® and *EnergyPlus*™ to predict the biological energy harvest (E) with such a system on an hourly basis. The model examined the impact of design metrics of double-skin façades, including cavity width (W) and bioreactors tilt angle (β), on the received irradiation in different urban forms with variable densities and building heights. The output from shading analysis was fed to a heat transfer sub-model in order to balance convection, radiation, and energy generation. Results showed that bioreactors integrated into double-skin façades collected less irradiation by up to 53.1% compared to single-skin façades. However, such façades managed to cut down the heating requirements for the water in the microalgae medium by 60.4% (from 272.9 W/m to 108.2 W/m). Higher density contexts decreased E/E_{max} from 53.5% to 27.8%. This was compensated in high-rise buildings by restoring E/E_{max} to 63.9%. Using artificial neural networks, the mean error associated with shading factor estimation was 3.7%. The study concluded that E was maximum in low-density contexts with high-rise buildings having W=1.2 m and β=45°.

KEYWORDS:

Double-skin façades; Microalgae photobioreactors; Heat transfer; Building performance; Biomass generation.

1. INTRODUCTION

Globally, buildings are responsible for 40% of the total energy consumption and contribute to about 30% of the CO_2 emissions [1]. Renewable sources' integration into buildings has been the scope of recent research to address this challenge [2,3]. In particular, photobioreactors (PBRs) integrated into buildings have many merits, such as biomass production, O_2 generation, CO_2 sequestration, and wastewater treatment [4]. Annually, flat panel PBRs generated 22.7 kWh/m^2 of methane and 30 kWh/m^2 of heat when added to building façades [5]. Other attempts of PBRs inclusion in buildings achieved a biomass production of 2.3 kg/m^2.year and CO_2 bio-fixation of 31.7 kg/m^2.year [6]. Nevertheless, previous attempts didn't investigate the performance of PBRs in extremely cold regions. The relatively low temperature in such climates led to very low growth rates of microalgae [7].

All attempts to integrate PBRs in buildings considered only single-skin façades (SSFs) [5,6]. However, double-skin façades (DSFs) offered the flexibility to host energy-efficient technologies [8], in addition to adjusting heat transfer through building envelopes [9,10]. The thermal performance of DSFs, in terms of heat gain and airflow within the cavity, was analyzed by finite volume approaches [11]. Nonetheless, this was restricted to venetian blinds without the integration of any renewable sources. DSFs were examined by integral models to evaluate the impact of cavity size as well as ventilation openings' type and width on the heat gain [12]. Such models required less time and provided adequate accuracy [12]. Temperature prediction in DSFs had a deviation of 2 ℃ by the same models [13]. Other integral models aided by MATLAB [8,14], and DesignBuilder [15], were further employed to assess the performance of renewable panels inside DSFs. Such systems managed to provide office buildings with 120 kWh/year [14]. However, the investigated panels were limited to photovoltaics integrated into the outer skin of DSFs. The integration of PBRs into the inner skin can help preserve the required thermal energy for optimum performance in cold climates [16]. Such inclusion will require considering the reduction in solar irradiation due to shading from the DSF elements.

Shading analysis is essential in modeling any solar harvesting techniques integrated into building façades. Shading imposed on buildings decreases solar heat gain and reduces cooling demand [17]. However, adding PBRs to façades requires maximizing solar irradiation. Both self-shading of DSF elements or shading caused by urban contexts can reduce the power output to zero [18]. Using GIS database, optimal building design increased solar irradiation by 74.2% on façades [19]. However, this method required accessibility to geographic data which could be nonexistent for some locations [20,21]. This was avoided by employing hand-coded vectorial models which achieved the same objective using different platforms such as *Python*, and *MATLAB* [22]. Vectorial models were quite satisfactory regarding elapsed time, results' accuracy, and integration into broader projects [22–26]. However, these models were applied to very special cases such as: 1) one façade overlooking a single building [22,26]; 2) multiple buildings having the same height [23]; or 3) a single point centered in a circular building [24] or within three buildings [25].

Machine learning approaches were also applied to estimate the shading impact in cities [27,28]. Such tools were reported to be problematic when orientation or sky view factor were considered among inputs [28]. The evaluated errors for calculating radiation were 18% and 37% in summer, and winter, respectively [28]. In light of the above, this study aims to evaluate the reduction in the solar gain of DSFs' inner layer compared to SSFs. The DSF cavity width and integrated PBRs' tilt angle will then be optimized for maximizing biomass energy generation. The study will also assess the DSFs' potential in preserving the thermal energy for PBRs in cold climates. Finally, this work will consider the impact of building height, surroundings' tilt, and urban density on the energy generated from the proposed system. Figure 1 shows the investigated DSF building along with the PBRs and the surrounding context.

2. METHODOLOGY

The present study examined a DSF system of the corridor type. The two variables defining the DSF geometry, in this case, were the cavity width (*W*) and the PBRs' tilt angle (*β*). Figure 2 shows the façade section with main dimensions and relevant heat transfer modes. The study imported weather data for Waterloo, ON, Canada from *EnergyPlus*™. Temperature, wind speed, and beam irradiation were then exported to *MATLAB*®, before performing thermal and shading simulations. To maximize solar irradiation, this work investigated South-oriented façades. The examined contexts were generalized by considering curvilinear forms (Figure 1). Streets in such an elliptical context are perfect circles for *A*=*B*, and linear for the extreme case when *B* >>> *A*.

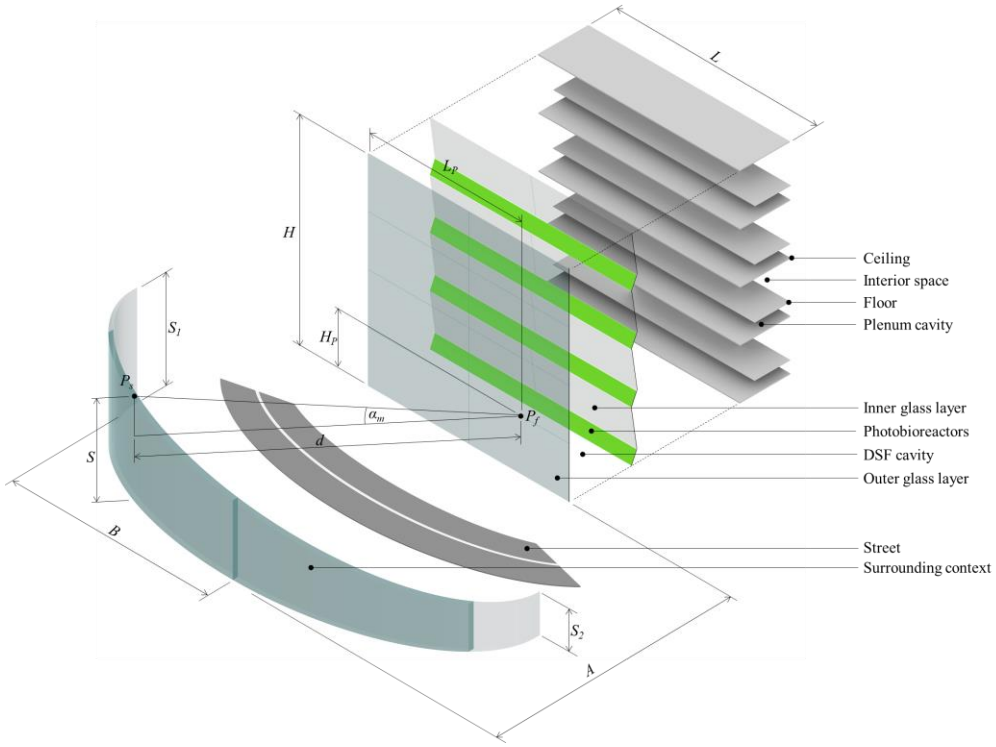

Figure 1. Examined parameters of the DSF, building, and surrounding context.

2.1. Heat transfer and energy generation

Cavity air in the DSF system was enclosed by five elements: cavity bottom, cavity top, inner glass layer, outer glass layer, and PBRs. Heat transfers by radiation between any pair of these elements at a rate of [29]

$$q_{rn,1-2} = \frac{\sigma(T_1^4 - T_2^4)}{\frac{1-\varepsilon_1}{\varepsilon_1 A_1} + \frac{1}{A_1 F_{1-2}} + \frac{1-\varepsilon_2}{\varepsilon_2 A_2}} \quad (1)$$

where $q_{rn,1\text{-}2}$ is the radiative heat transfer between elements 1 and 2. $F_{1\text{-}2}$ is the view factor between these elements. T, A, and ε are the temperature, area, and emissivity. σ is the Stefan-Boltzmann constant, W/m^2.K^4. Heat transfers by convection between fluids and solid surfaces according to [29]

$$q_{cn,s-f} = hA(T_s - T_f) \quad (2)$$

where $q_{cn,s\text{-}f}$ is the convective heat transfer between any surface and the adjacent fluid. h is the convection heat transfer coefficient, W/m^2.K. The temperature of each element in the DSF assembly was calculated by balancing the energy flows for this element. At steady-state conditions, the solar irradiation absorbed by PBRs ($\alpha_{PBRs}G_{PBRs}$) was partially transformed into biological energy (E) and thermal heat (q_{water}). Remaining energy was lost by convection to the cavity air ($q_{cn,PBRs\text{-}c}$) and by radiation to inner glass ($q_{rn,PBRs\text{-}ig}$), outer glass ($q_{rn,PBRs\text{-}og}$), cavity top ($q_{rn,PBRs\text{-}t}$) and cavity bottom ($q_{rn,PBRs\text{-}b}$). Therefore, the temperature of PBRs' walls was calculated from

$$\alpha_{PBRs}G_{PBRs} = q_{rn,PBRs-og} + q_{rn,PBRs-ig} + q_{cn,PBRs-c} + q_{rn,PBRs-t} + q_{rn,PBRs-b} + E + q_{water} \quad (3)$$

All temperatures of DSF elements were also unknowns in Equation 3. Heat balance was thus formulated for each element and all energy equations were solved simultaneously. Remaining energy balance equations were

$$\alpha_{og}G_{og} + q_{rn,ig-og} + q_{rn,PBRs-og} + q_{rn,t-og} + q_{rn,b-og} + q_{cn,c-og} = q_{rn,og-s} + q_{cn,og-a} \quad (4)$$

$$\alpha_{ig}G_{ig} + q_{rn,rw-ig} + q_{rn,PBRs-ig} + q_{cn,ra-ig} = q_{rn,ig-og} + q_{rn,ig-t} + q_{rn,ig-b} + q_{cn,ig-c} \quad (5)$$

$$q_{cn,ig-c} + q_{cn,PBRs-c} + q_{cn,t-c} + q_{cn,b-c} = q_{cn,c-og} \quad (6)$$

$$q_{rn,ig-t} + q_{rn,PBRs-t} + q_{rn,b-t} = q_{cn,t-c} + q_{rn,t-og} \quad (7)$$

$$\alpha_b G_b + q_{rn,ig-b} + q_{rn,PBRs-b} = q_{rn,b-t} + q_{cn,b-c} + q_{rn,b-og} \quad (8)$$

Figure 2 shows the heat exchange by radiation and convection between different DSF elements. All heat transfer coefficients were calculated using correlations from [29]. E was calculated from

$$E = \eta \times \tau_{og} \times I_b \times \cos\theta \times (1 - SF) \quad (9)$$

where η is the conversion efficiency from solar irradiation to biological energy. This efficiency was 9% as reported by [30]. τ_{og} is the transmissivity of outer glass layer. I_b is the hourly beam irradiation imported from weather files, W/m^2. θ is the PBRs' solar incidence angle, rad. SF is the shading factor or the shaded fraction of the total PBRs' area.

2.2. Shading impact

The solar energy received by the PBRs was directly impacted by the shading imposed by both surrounding buildings and DSF elements. This work considered the two factors for calculating SF by employing vectorial models. These models utilized basic trigonometry to perform a line search along the solar ray reaching a given point. The point was shaded if one object was detected in the search direction.

2.2.1. Shading in DSFs

The portion of PBRs receiving solar irradiation was dependent on both W and β in addition to the solar altitude angle (α). Figure 2 shows the impact of α on SF. when $\alpha \le \alpha_1$, PBRs were totally unshaded (SF=0). When $\alpha_1 \le \alpha \le \alpha_2$, the PBRs' shading factor (SF) was calculated by

$$SF = \overline{P_1P_2}/\overline{P_1P_3} \quad (10)$$

P_1 and P_3 were expressed as

$$\begin{bmatrix} P_1 \\ P_3 \end{bmatrix} = \begin{bmatrix} -L_{pl} \cot \beta & L_{pl} \\ 0 & 0 \end{bmatrix} \tag{11}$$

where L_{pl} is the plenum height, m. P_2 was calculated by finding the intersection point between the lines P_1P_3 and P_4P_5. P_4 and P_5 were expressed as

$$\begin{bmatrix} P_4 \\ P_5 \end{bmatrix} = \begin{bmatrix} W - L_{og} \cot \alpha & 0 \\ W & L_{og} \end{bmatrix} \tag{12}$$

where L_{og} is the outer glass height, m. PBRs were totally shaded (SF=1) when $\alpha \geq \alpha_2$.

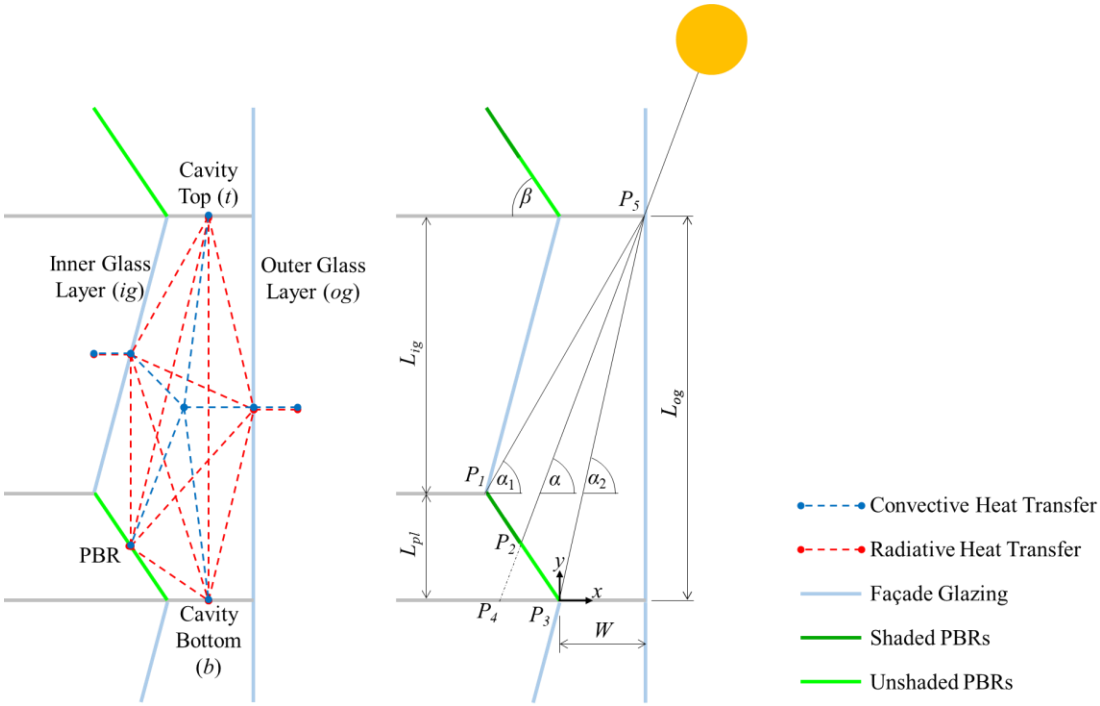

Figure 2. Left: Convective and radiative heat transfer modes of the DSF. Right: Parameters considered for investigating SF of PBRs integrated into DSFs.

2.2.2. Shading in urban contexts

Urban contexts with elliptical forms had minor and major axes of 2A and 2B. Figure 1 shows the tilt in such contexts with maximum, local, and minimum heights of S_1, S, and S_2, respectively. Each point on the façade (P_f) was investigated on an hourly basis to calculate the minimum solar altitude angle (α_m). When $\alpha < \alpha_m$, P_f was shaded by the surroundings, α_m was calculated from

$$\alpha_m = \tan^{-1}[(S - H_P)/d] \tag{13}$$

where H_P is the vertical distance between P_f and the ground, m. d is the horizontal distance between P_f and the intersection between the solar plan and the surroundings (P_s). As shown in Figure 3, d was calculated from

$$d^2 = x^2 + y'^2 \tag{14}$$

For all cases, the first term was identical to the x-coordinate of P_s. However, the second term (y') was dependent on the y-coordinate of P_s, L_P, and the hour angle (ω). For $\omega \leq 0$, y' was calculated from

$$y' = y - L_P + L/2 \tag{15}$$

For $\omega > 0$, y' was calculated from

$$y' = -y + L_P - L/2 \tag{16}$$

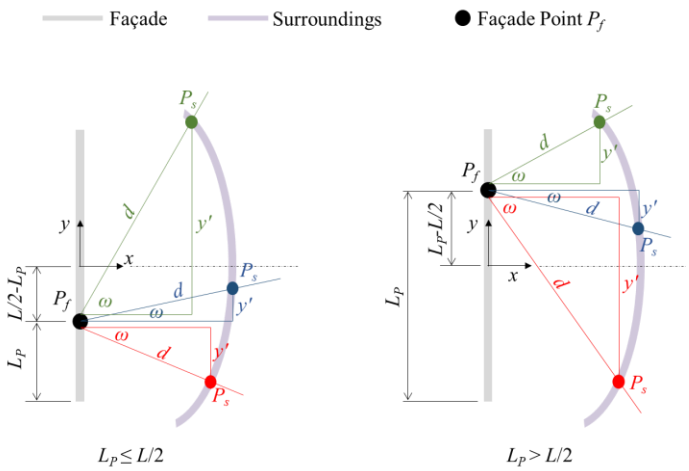

Figure 3. Plan view of the building façade and context for all possible combinations of ω and L_P.

2.2.3. Shading estimation using artificial neural networks (ANNs)

To investigate the potential of machine learning in shading prediction, the examined façade was divided into 400 elements (20×20). *SF* for all elements on the façade was expressed as a 2D matrix (M_1). The columns of M_1 were combined into a single column to form a column output $\boldsymbol{y} \in R^{400}$, which varied with the variables *A/L* and *B/L*. 34 points were generated with $\boldsymbol{x} \in R^2$ as an input, where $\boldsymbol{x}^T$=[*A/L B/L*], and $\boldsymbol{y}$ as an output. Afterward, a neural network was trained by 25 points, while the remaining 9 points were used to test the algorithm performance. To find the set of weights ($\boldsymbol{w}^h$ and $\boldsymbol{w}^o$), scale parameters ($\boldsymbol{\beta}^h$, $\boldsymbol{\beta}^o$), and shift parameters ($\boldsymbol{\theta}^h$, $\boldsymbol{\theta}^o$) for the hidden (^{h}) and output (^{o}) layers, the following objective function should be minimized

$$\min_{\boldsymbol{w}^h,\boldsymbol{w}^o,\boldsymbol{\beta}^h,\boldsymbol{\beta}^o,\boldsymbol{\theta}^h,\boldsymbol{\theta}^o} \frac{1}{2}\sum_{d=1}^{D}\left[\sum_{s=1}^{m}(y_{ds}-\phi_{ds})^2\right] \tag{17}$$

where

$$\phi_{ds} = \beta_s^o F_s^o\left(\sum_{j=1}^{l} w_{sj}^o \beta_j^h F_j^h\left(\sum_{i=1}^{n} w_{ji}^h x_{di} - \theta_j^h\right) - \theta_s^o\right) \tag{18}$$

y_{ds} is the exact output of the d^{th} point. $\boldsymbol{\phi}_{ds}$ is the output from the neural network algorithm of the d^{th} point. Finally, the updated weights and parameters, for both the hidden and output layers, were calculated from

$$\boldsymbol{w}^{k+1} = \boldsymbol{w}^k - \eta\left(\frac{\partial \boldsymbol{E}}{\partial \boldsymbol{w}}\right)^{\boldsymbol{k}} \tag{19}$$

$$\boldsymbol{\theta}^{k+1} = \boldsymbol{\theta}^k - \eta\left(\frac{\partial \boldsymbol{E}}{\partial \boldsymbol{\theta}}\right)^{\boldsymbol{k}} \tag{20}$$

$$\boldsymbol{\beta}^{k+1} = \boldsymbol{\beta}^k - \eta\left(\frac{\partial \boldsymbol{E}}{\partial \boldsymbol{\beta}}\right)^{\boldsymbol{k}} \tag{21}$$

3. RESULTS AND DISCUSSIONS

Assessment of irradiation (I_b) is essential for all solar harvesting applications. Figure 4 compares I_b received by PBRs integrated into SSFs or DSFs. Hourly simulations were performed for each month and box plots were generated. Each box plot shows one set of I_b received by PBRs with specific β and façade type. I_b received by SSFs and DSFs had a negligible difference between September and March. That's mainly due to the lower α in such a period. In summer, the deviation in I_b was almost 53.1% between SSFs and DSFs

because of higher α. The average I_b dropped from 344.5 W/m^2 in SSFs to 161.4 W/m^2 in DSFs for June. Lower β was more feasible in summer because of the same impact of α. This may give SSFs an advantage over DSFs in such a period. However, extremely hot days could have a negative impact on the performance of PBRs. In July, maximum I_b increased in SSFs by 83.5% (from 492.4 W/m^2 to 903.6 W/m^2) when β decreased from 90° to 45°. This percentage was estimated by [31] to be 80%. This deviation could be interpreted due to the different locations. In DSFs with W=2.4 m, this increment was from 393 W/m^2 to 562.8 W/m^2 due to shading effect.

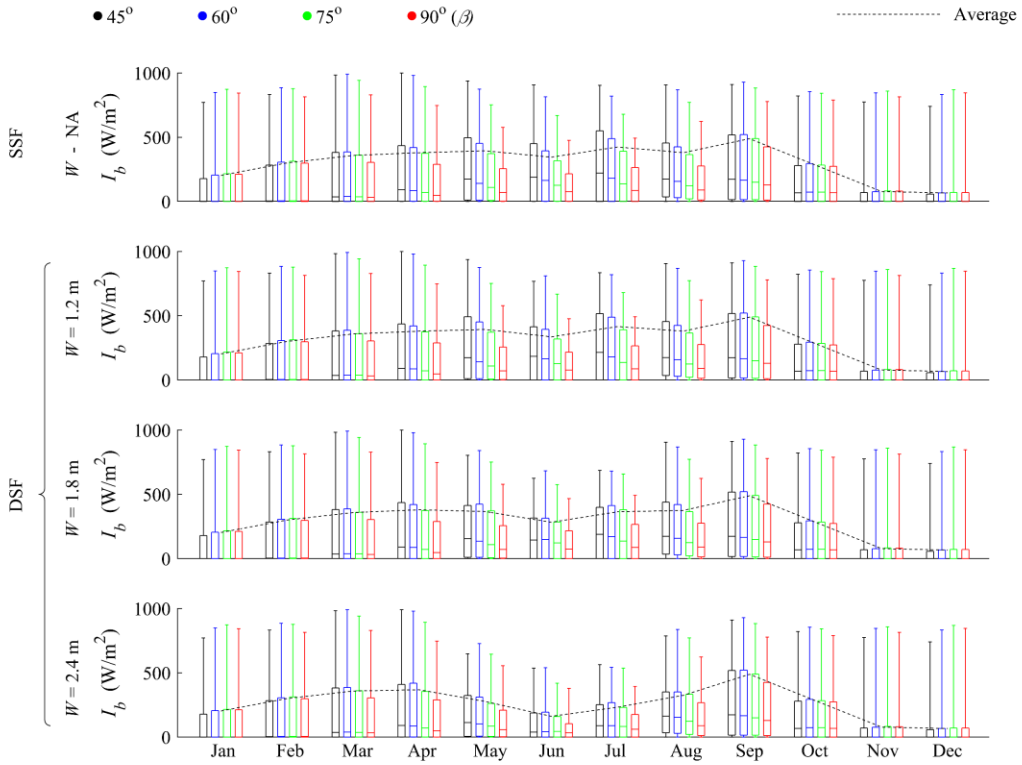

Figure 4. Variation of hourly I_b in each month for different façade systems and tilt angles.

Heat transfer and DSF shading models were coupled to calculate hourly E for each combination of β and W. Figure 5 shows the graphical optimization method applied to determine the optimum growth conditions. At β=30°, E decreased with W at an average rate of 1.8 W/m^2 per meter. This value dropped to 0.3 W/m^2 per meter for β=90°. The optimum β varied between 40° and 60° over the W range. Such a range for optimum β was quite significant as the examined location in this study has a latitude of 43°. DSF systems with W=0.6 m and β=45° offered the highest biomass generation with E=13.1 W/m^2. The optimum β estimated in a similar study examining a free-standing PBR was also 45° [32]. However, W=0.6 m decreased cavity accessibility, which is required for cleaning and maintenance [9]. Therefore, the optimum growth conditions were W=1.2 m and β=45°. That's because the variation of E was only within 3% for W ranging between 0.6 m and 1.2 m.

Although DSFs received lower I_b, less energy was required to keep the cultivation medium at the optimal temperature of 25 °C [16]. Figure 5 shows the thermal exchange with the medium water (q_{water}) and the associated temperature (T_{PBRs}) for both façade types. When q_{water} < 0, heat was required to maintain the set temperature. In January, q_{water} median for SSFs and DSFs were 272.9 W/m and 108.2 W/m, respectively. This showed that DSFs preserved 60.4% of the required thermal energy compared to SSFs. Such an impact of DSFs in terms of heat conservation was also observed in [10], where the heating demand was reduced by 39%. Moreover, PBRs in SSFs had a wider span of T_{PBRs} and q_{water}. In such a case, DSFs had a more stable operation as the fluctuation range of T_{PBRs} was 1.6 °C less than SSFs. In July, thermal energy was generated from SSFs and DSFs at rates of 41.4 W/m and 100.1 W/m. In this month, T_{PBRs} was in the ranges of 24 °C to 26.3 °C and 24.6 °C to 26.5 °C for both systems, respectively.

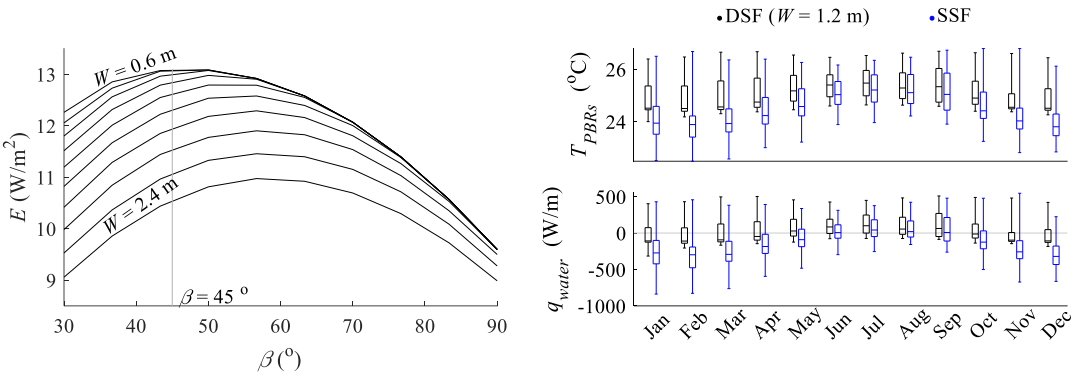

Figure 5. Left: Annual average E for DSF systems with different W and β. Right: Hourly variations of PBRs' wall temperature and generated/required heat for SSFs and the optimal DSF.

Density of urban contexts was expressed by the variables *A* and *B*. *A*/*L*=*B*/*L*=0.5 represented high density while *A*/*L*=*B*/*L*=0.9 represented low density. High-rise, mid-rise, and low-rise buildings were represented by *H*/*L*=2.0, 1.0, and 0.5, respectively. Figure 6 shows the impact of different surroundings on E/E_{max} by considering *A*, *B*, S_2, and *H*. Mid-rise buildings in flat surroundings were represented by *H*/*L*=1.0 and S_2/L=1.0. The results were consistent with [33] that high-density contexts had an inverse impact on energy generation from façades. However, increasing the façade height managed to mitigate such a deficiency. For instance, although E/E_{max} decreased from 53.5% in low-density contexts to 27.8% in high-density contexts, high-rise buildings with *A*/*L*=*B*/*L*=0.5 restored E/E_{max} to 63.9%. *A*/*L* had a higher impact on E/E_{max} compared to *B*/*L*. For *A*/*L*=0.7, E/E_{max} increased by 7.1% on average by increasing *B*/*L* from 0.5 to 0.9. Same increment in *A*/*L* boosted E/E_{max} by 12.7% for *B*/*L*=0.7. The surroundings' tilt had a higher impact on the generated energy compared to the buildings' density.

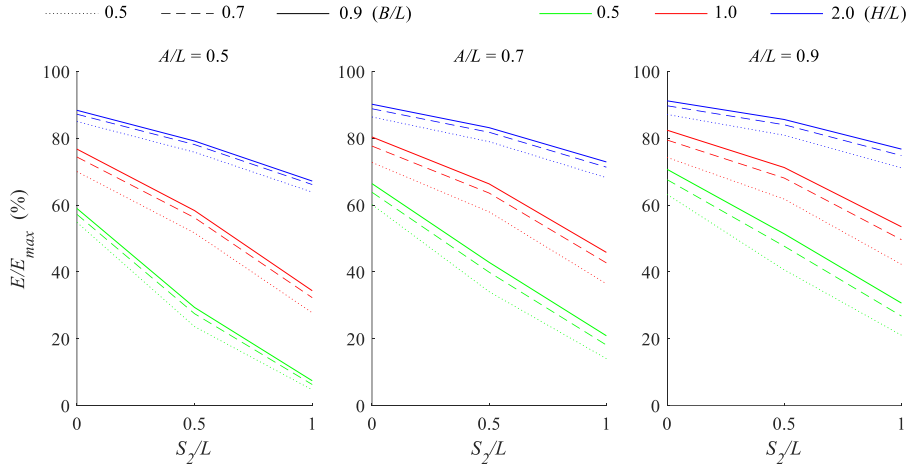

Figure 6. Variation of normalized biomass generation with different contexts.

The initial values of the set of weights ($\boldsymbol{w}^h$ and $\boldsymbol{w}^o$), scale parameters ($\boldsymbol{\beta}^h$, $\boldsymbol{\beta}^o$), and shift parameters ($\boldsymbol{\theta}^h$, $\boldsymbol{\theta}^o$) were all considered as ones. Afterward, different numbers of neurons in the hidden layer and different values of the fixed step (η) were tested. Figure 7 (a) shows the variation of the error with the number of iterations (k) for different numbers of neurons in the hidden layer and different fixed step sizes (η). A higher number of neurons didn't guarantee the best performance of the neural network algorithm. For a smaller number of neurons, a fixed step size of 0.1 was always faster in convergence and more accurate compared to other values. Consequently, the current neural network was constructed using 2 neurons in the hidden layer and the gradient optimization was carried out with a fixed step size of 0.1 during the training process. The contours of the 9 testing points were calculated using both the vectorial model and the trained neural network. The error was expressed as the absolute difference multiplied by 100. Figure 7 (b) shows the error contours for the 9 testing points. The lowest performance of the algorithm was noticed with $\boldsymbol{x}^T$=[*A*/*L B*/*L*]=[*0.55 0.55*] where the mean error in such case was 8%. However, the overall mean error was 3.7%.

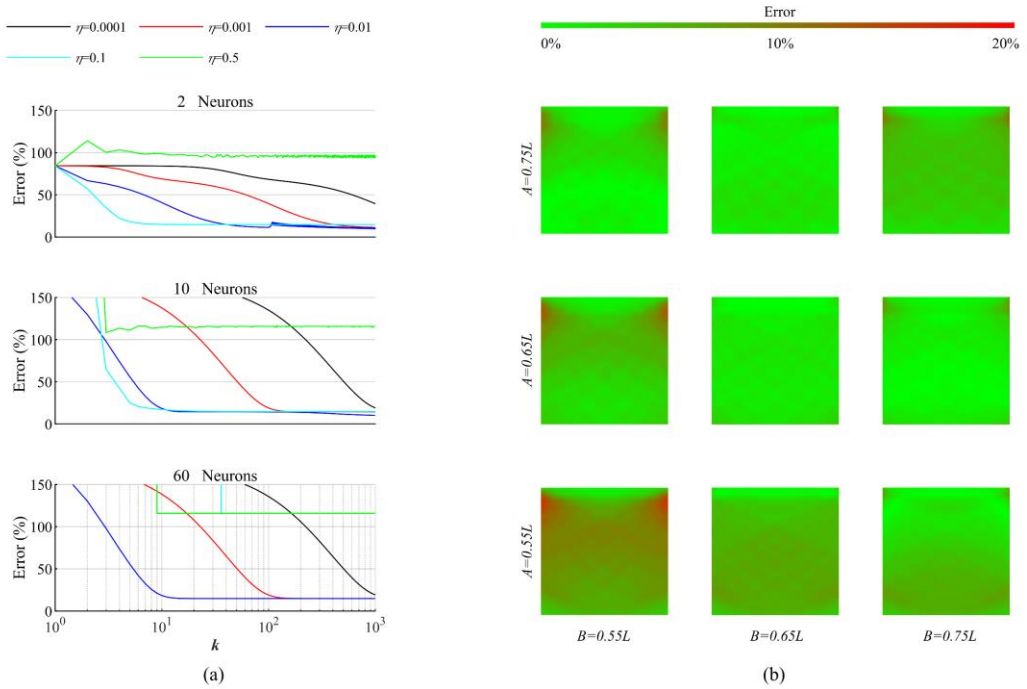

Figure 7. (a) Error variation with the number of iterations (k) for different numbers of neurons in the hidden layer and different fixed step sizes (η). (b) Error contours for the 9 testing points.

4. CONCLUSION

Sustainable buildings utilize various renewable sources for power generation and efficient energy consumption. Building-integrated PBRs represent one of the most promising solar harvesting technologies. However, the optimum design of PBRs, preserving the panels' heat, and the impact of surrounding environments are still being investigated. This work proposed an integral model for the assessment of PBRs integrated into DSF systems. The study comprised three sub-models for analyzing heat transfer by convection and radiation, assessing DSF shading, and examining different urban contexts. Panels were added to the inner layer to decrease the energy required for maintaining the medium at 25 °C. Such inclusion also reinforced the DSF thermal buffer by directing the water heat loss to the cavity air. Recent literature investigated the performance of PBRs with SSFs [5,6] or examined the inclusion of photovoltaics in DSFs [8,14,15]. This study optimized the integration of PBRs in DSFs, assessed the DSFs' impact on preserving the panels' heat, and evaluated the effect of surrounding contexts on generated energy. Highest biomass production of 13.1 W/m^2 was achieved by systems having W=0.6 m and β=45°. However, systems with W=1.2 m and β=45° offered adequate space for cavity maintenance and cleaning with less than 3% bioenergy loss. Generated biomass is considered as a sustainable oil source that can replace liquid fossil fuels consumed to fuel the building.

Regarding thermal energy conservation using DSFs, the optimized system required heat input in winter at rates of 272.9 W/m and 108.2 W/m for SSFs and DSFs, respectively. In summer, the system generated heat at rates of 41.4 W/m and 100.1 W/m for both façade types. Although shading vectorial models in recent literature were restricted to very special cases [22–26], the present study modeled a general urban grid with the flexibility of varying heights and tilts. In tilted surroundings, E median was higher by 70.9% compared to flat surroundings (5.5 W/m^2 compared to 9.4 W/m^2). PBRs in high-density contexts had E/E_{max}=27.8%. This was increased to either 53.5% or 63.9% by installing the panels in low-density contexts or high-rise buildings, respectively. This work investigated the potential of machine learning in shading prediction. The estimated mean error value was 3.7%. Such results promoted the feasibility of collecting solar irradiation data from physical buildings to train the developed neural network model. Consequently, this will avail the model to predict the solar heat gain to buildings in various neighborhoods with a relatively accepted error. Future work should consider detailed modeling of the chemical kinetics driving the photosynthetic process in PBRs. It is also recommended to investigate different designs of DSFs and evaluate the corresponding impact on heat and bioenergy generation.

5. REFERENCES

[1] L. Yang, H. Yan, J.C. Lam, Thermal comfort and building energy consumption implications – A review, Applied Energy. 115 (2014) 164–173. https://doi.org/10.1016/j.apenergy.2013.10.062.

[2] A. Ahmed, T. Ge, J. Peng, W.-C. Yan, B.T. Tee, S. You, Assessment of the renewable energy generation towards net-zero energy buildings: A review, Energy and Buildings. 256 (2022) 111755. https://doi.org/10.1016/j.enbuild.2021.111755.

[3] T. Ahmad, H. Zhang, B. Yan, A review on renewable energy and electricity requirement forecasting models for smart grid and buildings, Sustainable Cities and Society. 55 (2020) 102052. https://doi.org/10.1016/j.scs.2020.102052.

[4] M. Talaei, M. Mahdavinejad, R. Azari, Thermal and energy performance of algae bioreactive façades: A review, Journal of Building Engineering. 28 (2020). https://doi.org/10.1016/j.jobe.2019.101011.

[5] A. Trombadore, B. Paludi, M. D'Ostuni, Adaptive Design of Green Facades and Vertical Farm: Examples of Technological Integration of Microalgae for Energy Production in Resilient Architecture, in: 2022: pp. 273–294. https://doi.org/10.1007/978-3-030-68556-0_10.

[6] J. Pruvost, B.L. Gouic, J. Legrand, Symbiotic integration of photobioreactors in a factory building façade for mutual benefit between Buildings and Microalgae Needs, in: 21st International Congress of Chemical and Process Engineering CHISA 2014 Prague 17th Conference on Process Integration, Modelling and Optimisation for Energy Saving and Pollution Reduction PRES 2014, Praha, Czech Republik, 2014.

[7] J.N. Young, K. Schmidt, It's what's inside that matters: physiological adaptations of high-latitude marine microalgae to environmental change, New Phytologist. 227 (2020) 1307–1318. https://doi.org/10.1111/nph.16648.

[8] M. Shakouri, H. Ghadamian, S. Hoseinzadeh, A. Sohani, Multi-objective 4E analysis for a building integrated photovoltaic thermal double skin Façade system, Solar Energy. 233 (2022) 408–420. https://doi.org/10.1016/j.solener.2022.01.036.

[9] S. Barbosa, K. Ip, Perspectives of double skin façades for naturally ventilated buildings: A review, Renewable and Sustainable Energy Reviews. 40 (2014) 1019–1029. https://doi.org/https://doi.org/10.1016/j.rser.2014.07.192.

[10] Y.B. Yoon, B. Seo, B.B. Koh, S. Cho, Heating energy savings potential from retrofitting old apartments with an advanced double-skin façade system in cold climate, Frontiers in Energy. 14 (2020) 224–240. https://doi.org/10.1007/s11708-020-0801-1.

[11] S. Zeyninejad Movassag, K. Zamzamian, Numerical investigation on the thermal performance of double glazing air flow window with integrated blinds, Renewable Energy. 148 (2020) 852–863. https://doi.org/10.1016/j.renene.2019.10.170.

[12] Z. Su, X. Li, F. Xue, Double-skin façade optimization design for different climate zones in China, Solar Energy. 155 (2017) 281–290. https://doi.org/10.1016/j.solener.2017.06.042.

[13] F. Xue, X. Li, A fast assessment method for thermal performance of naturally ventilated double-skin façades during cooling season, Solar Energy. 114 (2015) 303–313. https://doi.org/10.1016/j.solener.2015.01.040.

[14] Z. Ioannidis, A. Buonomano, A.K. Athienitis, T. Stathopoulos, Modeling of double skin façades integrating photovoltaic panels and automated roller shades: Analysis of the thermal and electrical performance, Energy and Buildings. 154 (2017) 618–632. https://doi.org/10.1016/j.enbuild.2017.08.046.

[15] F. Ascione, N. Bianco, F. de Rossi, T. Iovane, G.M. Mauro, Are transparent double-skin facades effective for energy retrofit? Answers for an office building - with and without photovoltaic integration, Energy Sources, Part A: Recovery, Utilization, and Environmental Effects. 44 (2022) 257–271. https://doi.org/10.1080/15567036.2022.2042430.

[16] I. Havlik, P. Lindner, T. Scheper, K.F. Reardon, On-line monitoring of large cultivations of microalgae and cyanobacteria, Trends in Biotechnology. 31 (2013) 406–414. https://doi.org/10.1016/j.tibtech.2013.04.005.

[17] J. Futcher, G. Mills, R. Emmanuel, Interdependent energy relationships between buildings at the street scale, Building Research and Information. 46 (2018) 829–844. https://doi.org/10.1080/09613218.2018.1499995.

[18] A. Aronescu, J. Appelbaum, Shading on photovoltaic collectors on rooftops, Applied Sciences (Switzerland). 10 (2020). https://doi.org/10.3390/APP10082977.

[19] T. A.l. Martins, L. Adolphe, L. E.g. Bastos, From solar constraints to urban design opportunities: Optimization of built form typologies in a Brazilian tropical city, Energy and Buildings. 76 (2014) 43–56. https://doi.org/10.1016/j.enbuild.2014.02.056.

[20] P. Redweik, C. Catita, M. Brito, Solar energy potential on roofs and facades in an urban landscape, Solar Energy. 97 (2013) 332–341. https://doi.org/10.1016/j.solener.2013.08.036.

[21] C. Chatzipoulka, R. Compagnon, M. Nikolopoulou, Urban geometry and solar availability on façades and ground of real urban forms: using London as a case study, Solar Energy. 138 (2016) 53–66. https://doi.org/10.1016/j.solener.2016.09.005.

[22] A. Márquez-García, M. Varo-Martínez, R. López-Luque, New model for the estimation of solar radiation on façades in urban environments, Renewable Energy and Power Quality Journal. 1 (2014) 729–734. https://doi.org/10.24084/repqj12.468.

[23] J. Esclapés, I. Ferreiro, J. Piera, J. Teller, A method to evaluate the adaptability of photovoltaic energy on urban façades, Solar Energy. 105 (2014) 414–427. https://doi.org/10.1016/j.solener.2014.03.012.

[24] M. Tripathy, S. Yadav, P.K. Sadhu, S.K. Panda, Determination of optimum tilt angle and accurate insolation of BIPV panel influenced by adverse effect of shadow, Renewable Energy. 104 (2017) 211–223. https://doi.org/10.1016/j.renene.2016.12.034.

[25] S. Yadav, C. Hachem-Vermette, S.K. Panda, G.N. Tiwari, S.S. Mohapatra, Determination of optimum tilt and azimuth angle of BiSPVT system along with its performance due to shadow of adjacent buildings, Solar Energy. 215 (2021) 206–219. https://doi.org/10.1016/j.solener.2020.12.033.

[26] K. Yu, Y. Chen, D. Wang, Z. Chen, A. Gong, J. Li, Study of the seasonal effect of building shadows on urban land surface temperatures based on remote sensing data, Remote Sensing. 11 (2019). https://doi.org/10.3390/rs11050497.

[27] S. Salcedo-Sanz, C. Casanova-Mateo, A. Pastor-Sánchez, M. Sánchez-Girón, Daily global solar radiation prediction based on a hybrid Coral Reefs Optimization – Extreme Learning Machine approach, Solar Energy. 105 (2014) 91–98. https://doi.org/10.1016/j.solener.2014.04.009.

[28] A. Vartholomaios, A machine learning approach to modelling solar irradiation of urban and terrain 3D models, Computers, Environment and Urban Systems. 78 (2019) 101387. https://doi.org/10.1016/j.compenvurbsys.2019.101387.

[29] S.L. Adrienne, F. Incropera, T. Bergman, D.P. Dewitt, Fundamentals of Heat and Mass Transfer, 7th ed., John Wiley & Sons, Inc., Jefferson City , USA, 2011.

[30] M.T. Araji, I. Shahid, Symbiosis optimization of building envelopes and micro-algae photobioreactors, Journal of Building Engineering. 18 (2018) 58–65. https://doi.org/10.1016/j.jobe.2018.02.008.

[31] J. Pruvost, B. le Gouic, O. Lepine, J. Legrand, F. le Borgne, Microalgae culture in building-integrated photobioreactors: Biomass production modelling and energetic analysis, Chemical Engineering Journal. 284 (2016) 850–861. https://doi.org/10.1016/j.cej.2015.08.118.

[32] J. Pruvost, J.F. Cornet, F. le Borgne, V. Goetz, J. Legrand, Theoretical investigation of microalgae culture in the light changing conditions of solar photobioreactor production and comparison with cyanobacteria, Algal Research. 10 (2015) 87–99. https://doi.org/10.1016/j.algal.2015.04.005.

[33] X. Chen, H. Yang, J. Peng, Energy optimization of high-rise commercial buildings integrated with photovoltaic facades in urban context, Energy. 172 (2019) 1–17. https://doi.org/10.1016/j.energy.2019.01.112.